

Twin Antenna X-Band Interferometry

Radio Astronomy Laboratory

ANDREW SHERIDAN

SHARKS IN SPACE

PROFESSOR AARON PARSONS

April 6, 2018

Abstract

We observe the Orion Nebula, the Sun, and the Moon with a two antenna X-Band Interferometer. Using point source fringe amplitudes at a known declination we determine the North-South baseline separation distance between our antenna to be $1.436 \text{ m} \pm 0.005 \text{ m}$, and the East-West baseline to be $14.745 \text{ m} \pm 0.0004 \text{ m}$. We find the length difference in the cables connecting the antenna to the electronics to be 10.3 cm . We compute the radii of the Sun and the Moon and find their values to be 0.566° and 0.467° respectively.

1 Introduction

Interferometers have been staples of scientific inquiry since Albert Michelson's first experiments with optical interferometry well over 120 years ago. These powerful tools allow us to produce information by collecting signals from disparate points and mixing them together and analyzing the result. A major benefit to interferometers is that by extending the separation distance between the sensors we can increase the effective size of the interferometer. As we increase the separation distance, or baseline, the collecting power increases linearly with the number of telescopes, while the angular resolution increases geometrically.

We observe three targets with the interferometers on the roof of New Campbell Hall, University of California, Berkeley. We cover the configuration of the signal chain in §2.1 and a brief overview of the relevant mathematics in §2.3. We observe a point source in §3 and use the data to classify certain parameters of our interferometer. We observe two resolved sources in §4 and compute their radii. Finally in §5 we discuss the implications of our findings.

2 Methods

2.1 Hardware

On the roof of New Campbell Hall are two 1 meter X-Band antenna housed in dishes about 1 meter in diameter, separated as far apart as possible on the roof, approximately 15 meters. The incoming signal is routed to the 5th floor undergraduate radio astronomy laboratory, and into various components. The incoming signal has frequency $\nu = 10.7 \text{ GHz}$, and is brought to baseband by the various mixers and local oscillators detailed in Table 4 (page 10) and Figure 17 (page 11).

2.2 Software

The output of the signal chain feeds into a digital multimeter, which we can access via `ugradio.HPM`. The interferometer can be directed using `ugradio.interf`. To obtain horizon to horizon time series signal data this author wrote the script `observation_function.py`, which can be used to point at the Moon, the Sun, or other sources. The default settings for the script re-points the interferometer every 10 seconds, and instructs the multimeter to record data every 1 second, saving data every 300 seconds. New pointing coordinates are calculated on the fly, for whatever the current time is. Various other functions and scripts were created to support the observation function, for loading and saving of data, and other tasks.

2.3 Theory

A basic layout of a two antenna interferometer is shown in Figure 1. The time delay that the separation induces is

$$\tau_{\text{tot}} = \tau_g(\alpha^\circ) + \tau_c, \quad (1)$$

where α° = hour angle, τ_g is the geometric delay, and τ_c is the physical cable delay caused by the different length cables. The geometric term τ_g can be written as a function of α° , τ_g' (Equation 25, page 4). Similarly the constant terms can be grouped together into τ_c' (Equation 20, page 4).

The signals that are received by the two antenna oscillate based on the frequency ν ,

$$E_1(t) = \cos(2\pi\nu t) \quad \& \quad E_2(t) = \cos(2\pi\nu[t + \tau_{\text{tot}}]) \quad (2)$$

The interferometer signal chain multiplies these two signals together. After some light trigonometry and dropping of terms that average to zero, we arrive at the fringe amplitudes

$$F(\alpha^\circ) = \cos(2\pi\nu[\tau_g' + \tau_c']) \quad (3)$$

which easily expands into

$$F(\alpha^\circ) = \cos(2\pi\nu\tau_c') \cos(2\pi\nu\tau_g') - \sin(2\pi\nu\tau_c') \sin(2\pi\nu\tau_g'). \quad (4)$$

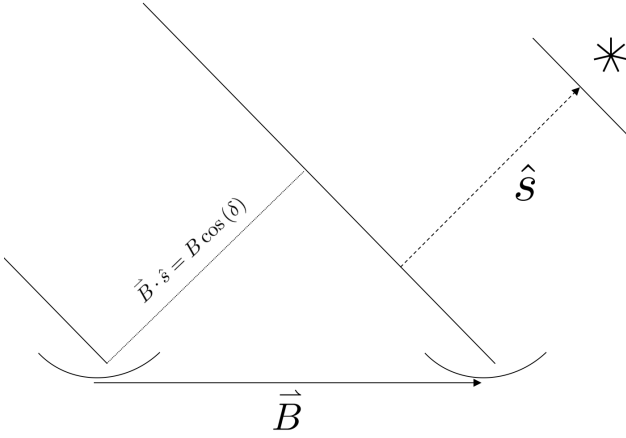


Figure 1: Geometry of a two antenna interferometer. The two dishes are the antenna, the solid vector pointing towards the star is the unit vector \hat{s} . The long solid lines are plane waves emanating from the source, while the dash line represents the geometric separation distance between the antenna. The source is considered to be so far away that the unit vector that points towards it is the same for both antenna. Plane waves from the source strike one antenna before the other, introducing a time delay.

Equation 4 represents the fringe amplitudes we expect to read with our multimeter when we make our observations. The corresponding fringe frequencies f_f are laid out in equation 26, page 4, and are also a function of (α°) .

3 Point Source

3.1 Orion Nebula Observation

The Orion Nebula is a region of star formation approximately 1500 lightyears away [2] and is visible to the naked eye in the constellation Orion on a clear night. It has coordinates $(\alpha, \delta)_{2000} = (83.82^\circ, -5.39^\circ)$. We observe the Orion Nebula for 10 hours on March 23, 2018, sampling the fringe amplitude every second. In Figure 2 we note a general upwards trend in the data. Because of the trigonometric nature of the expected fringe amplitudes, we suspect this is an equipment artifact but have no real explanation for the phenomenon.

The large number of samples allows us to fit a high order polynomial to the data without fear of over fitting. We subtract this fit from the data to force the data closer to be closer to theory. In Figure 3 we see this was only relatively successful.

3.2 Orion Nebula Fringe Frequencies

To ascertain whether or not we are truly observing our target, we look for fringe frequencies. Our time series data consists of just over 36 000 fringe amplitudes. To find the fringe frequencies hidden in the data we will compute multiple power spectra. If we have time series data with of a signal that oscillates at a steadily changing frequency f_f we can compute the power spectrum of many different windows in the data and should see peaks at the frequencies f_f . In Figure 4 we present

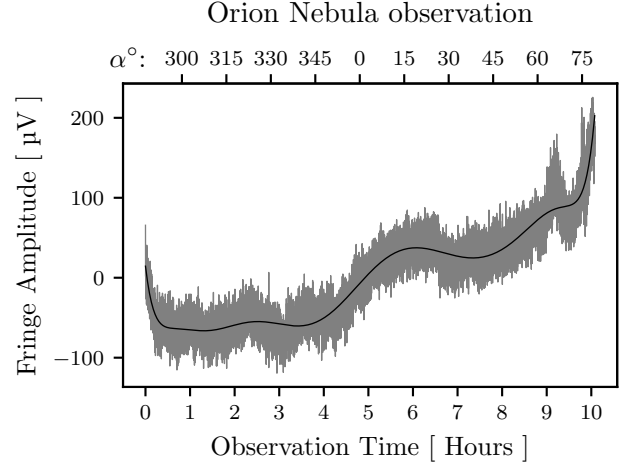


Figure 2: Fringe amplitudes collected during a 10 hour observation of the Orion Nebula, with a 12th degree polynomial fitted to the data. The upper axis α° represents the equivalent hour angle in degrees, do not confuse hour angle α° with the right ascension α . We subtract the mean of the data to eliminate a DC offset introduced by our equipment. The wavy upwards trend is unexpected, but is most likely also an equipment artifact. If we subtract the polynomial from the data we may reduce this effect. The data is of quite a low amplitude, further analysis must be done to be certain we have truly observed the Orion Nebula.

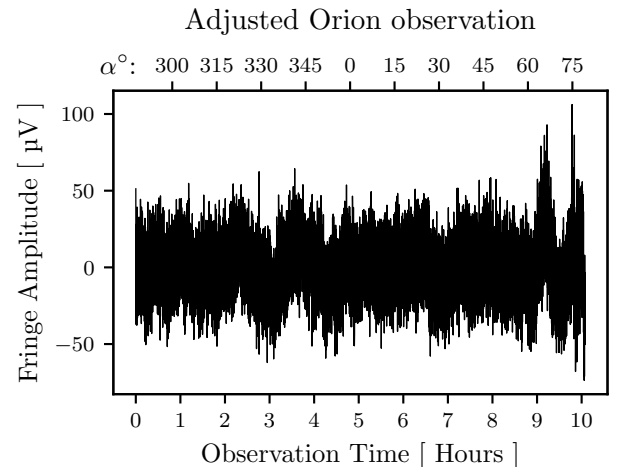


Figure 3: Orion Nebula observation fringe amplitudes minus a 12th degree polynomial fit. The adjustment was relatively successful. The general upwards trend has been largely eliminated, though some bumpy behavior remains.

36000 spectra. Each row represents a power spectrum calculated using a 1200 second window. We compute a spectrum for a window, then increment the window start time by one second, and compute a new spectrum. It is clear from the figure that we have not successfully eliminated the DC offset, as a dark line showing high power is visible at 0 Hz. Though difficult to make out, there are also arcing lines of strong power that are our fringe frequencies f_f . As predicted, they begin at a low frequency at the start of the observation and increase until the source is overhead, then decrease until the end of the observation.

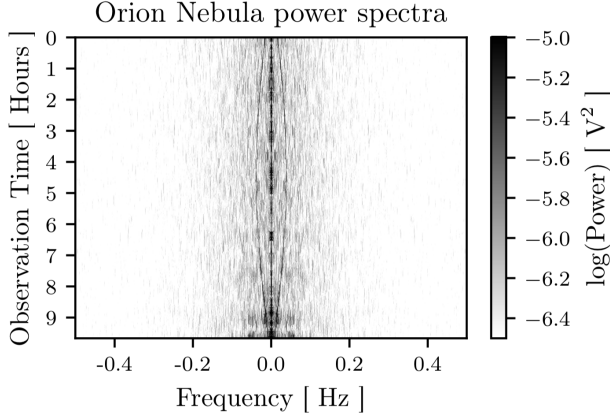


Figure 4: 36 000 separate power spectra, each representing a 1200 second window. By using a large window and incrementing the starting position of each window by one second we produce a large number high resolution power spectra. The dark line at 0 Hz is our unsuccessfully eliminated DC offset. The lines that arc from 0 Hz to 0.05 Hz and back are our fringe frequencies f_f .

3.3 Interferometer Calibration

Now that we are certain that we observed our target point source, and assuming that we take the coordinates of the target to be exact and fixed quantities, we can compute various parameters for our interferometer. The fringe amplitude for a point source can be found by rewriting equation 4,

$$F(\alpha^\circ) = A \cos(2\pi\xi) + B \sin(2\pi\xi) \quad (5)$$

where A and B are unknown coefficients.

Unless the source is directly ahead, the plane waves coming from our point source strike the nearer antenna first, causing one signal to be intercepted before the other. This time delay corresponds to the antenna separation distances, and is embedded in ξ .

$$\xi = \left[\frac{B_{\text{ew}}}{\lambda} \cos(\delta) \right] \sin(\alpha^\circ) + \left[\frac{B_{\text{ns}}}{\lambda} \sin(L) \cos(\delta) \right] \cos(\alpha^\circ) \quad (6)$$

Here, B_{ew} is the East-West separation of the antennas, while B_{ns} is the North-West separation, and L is the latitude of the interferometer. To simplify ξ we define two dimensionless quantities which are functions of the baselines:

$$Q_{\text{ew}} = \frac{B_{\text{ew}}}{\lambda} \cos(\delta) \quad \& \quad Q_{\text{ns}} = \frac{B_{\text{ns}}}{\lambda} \sin(L) \cos(\delta) \quad (7)$$

$$\Rightarrow \xi = Q_{\text{ew}} \sin(\alpha^\circ) + Q_{\text{ns}} \cos(\alpha^\circ) \quad (8)$$

3.4 Brute Force Least Squares

To determine the baseline distances, which are now embedded in the Q values, we fit Equation 5 to the fringe amplitudes in Figure 3. Due to the nonlinear nature of Equation 5, we use a brute force method to determine a best fit. We guess a pair of Q values and then perform a standard least squares fit for the unknown coefficients A and B .

Using matrices this is a speedy process. We define the $m \times 1$ column vector of the measured fringe amplitudes \vec{b} , the 2×1 column vector of the unknown coefficients

$$\vec{x} = \begin{bmatrix} A \\ B \end{bmatrix} \quad (9)$$

and the $m \times 2$ matrix of the trigonometric terms

$$\mathbf{M} = [\cos(2\pi\xi) \quad \sin(2\pi\xi)] \quad (10)$$

The $m \times 1$ column vector of the fitted fringe amplitudes \vec{y} is found via simple linear algebra

$$\mathbf{M}\vec{x} = \vec{b} \quad (11)$$

$$\vec{x} = (\mathbf{M}^T \mathbf{M})^{-1} \mathbf{M}^T \vec{b} \quad (12)$$

$$\vec{y} = \mathbf{M}\vec{x} \quad (13)$$

For each fit we compute the sum of the squares of the residuals, S^2 :

$$S^2 = \frac{1}{m-2} \sum_{i=1}^m (b_i - y_i)^2 \quad (14)$$

We store the value and then guess a new pair of Q values to recompute S^2 . Figure 5 shows the result of numerous iterations of this process.

3.4.1 Baselines

Using the minimum Q values found with Figure 5, we solve for the baselines in Equation 7 to find

$$B_{\text{ew}} = 14.745 \text{ m} \quad (15)$$

$$B_{\text{ns}} = 1.436 \text{ m} \quad (16)$$

3.4.2 Baseline Uncertainties

The baseline values are computed using found values of Q , so to find the error on the baseline we must first find the errors on Q . Fortunately this is not too difficult. At its minimum, the grid of S^2 values has a curvature that can be defined by a matrix of second partial derivatives

$$\mathbf{H} = \begin{bmatrix} \frac{1}{2} \frac{\partial^2 S^2}{\partial Q_{\text{ew}}^2} & \frac{\partial^2 S^2}{\partial Q_{\text{ew}} \partial Q_{\text{ns}}} \\ \frac{\partial^2 S^2}{\partial Q_{\text{ew}} \partial Q_{\text{ns}}} & \frac{1}{2} \frac{\partial^2 S^2}{\partial Q_{\text{ns}}^2} \end{bmatrix} \quad (17)$$

To compute these partial derivatives we make judicious use of `numpy.diff()`, iterating through the grid of S^2 in the appropriate directions. The inverse of \mathbf{H} is the covariance matrix for Q_{ew} and Q_{ns} , and the diagonal terms represent their error.

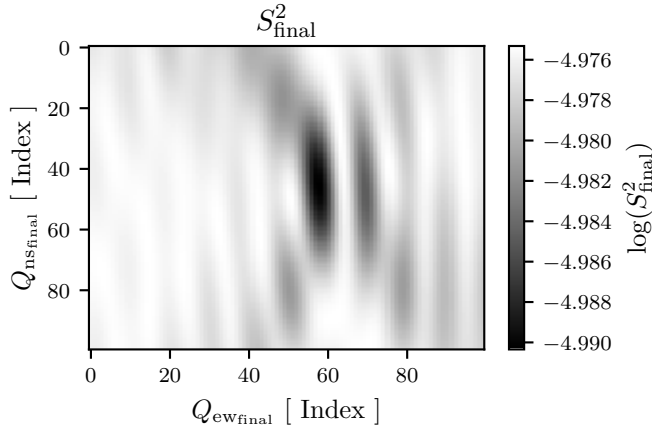


Figure 5: 10 000 values of S^2 . Each value is found using a unique pair of Q values. These values represent the fourth iteration of this process. For each iteration, two ranges of 100 Q values were used, and the darkest location in the image was noted. In the next iteration the bounds of the Q ranges were moved closer to the dark spot, though the number of values remained constant. The indices of the minimum S^2 value will provide the best fit values of Q_{ew} and Q_{ns} .

With these errors for the Q values we can compute the uncertainties on the baseline measurements with standard error propagation techniques [4].

$$\sigma_{B_{ns}} = 0.005 \text{ m} \quad (18)$$

$$\sigma_{B_{ew}} = 0.001 \text{ m} \quad (19)$$

3.4.3 Time Delay

The baseline measurements allow us to compute the geometric time delay embedded in ξ , as well as the time delay introduced by the differing lengths of the cables connecting our antennas to the rest of the signal chain. This cable delay τ_c is

$$\tau_c = \tau'_c + \frac{B_{ns}}{c} \cos(L) \sin(\delta), \quad (20)$$

with the speed of light c . Earlier we found values of A and B , these unknown constants are trigonometric terms that have τ'_c embedded in them. Now we use those to find τ'_c and in turn τ_c .

$$A = \cos(2\pi\nu\tau'_c) \quad \& \quad B = -\sin(2\pi\nu\tau'_c) \quad (21)$$

$$\frac{-B}{A} = \tan(2\pi\nu\tau'_c) \quad (22)$$

$$\tau'_c = \frac{\arctan\left(\frac{-B}{A}\right)}{2\pi\nu} \quad (23)$$

$$\tau'_c = 0.0123 \text{ ns}$$

Plugging the various values into Equation 20 gives

$$\tau_c = -0.343 \text{ ns} \quad (24)$$

which translates to a cable length differential of 10.3 cm.

The geometric delay in ξ varies based on the position of the source in the sky. When $\alpha^\circ = 0^\circ$, the delay is zero because the plane wave strikes both antennas at the same time. As α° moves away from 0° , the geometric delay changes.

$$\tau'_g = \left[\frac{B_{ew}}{c} \cos(\delta) \right] \sin(\alpha^\circ) + \left[\frac{B_{ew}}{c} \sin(L) \cos(\delta) \right] \cos(\alpha^\circ) \quad (25)$$

The total time delay due to these effects is $\tau_{tot} = \tau'_g + \tau'_c$. For the Orion Nebula we generate Figure 6 and see that it matches the predicted behavior.

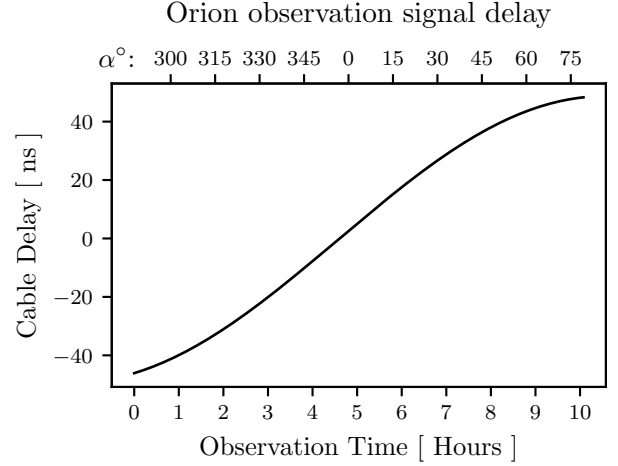


Figure 6: Total time delay due to geometric effects and the different lengths of cable the signal travels along. At $\alpha^\circ = 0^\circ$ the geometric delay vanishes and only the delay due to the cable remains. This figure would be similar for other targets in the sky.

3.5 Orion Nebula Fringe Frequencies, Redux

Having classified our interferometer, we compare the difficult to see fringe frequencies in Figure 4 to theoretical values. The theoretical values can be found with

$$f_{f,\text{theory}} = Q_{ew} \cos(\alpha^\circ) - Q_{ns} \sin(\alpha^\circ). \quad (26)$$

We must extract the observed fringe frequencies from the power spectra in Figure 4. We create a function that takes in an array and a threshold value. It iterates through the array, comparing elements with their neighbors and with the threshold. When a value is larger than the threshold and larger than all its neighbors, we save that value as a peak. For the Orion Nebula observation we expect two or three peaks for each spectra, two for the actual f_f we desire and a third for the strong DC offset we were unable to eliminate. For each spectrum, we set the threshold at the spectrum's maximum value, and repeatedly lower the value until the desired number of peaks are found. The located fringe frequencies are shown in Figure 7, and aside from some noise we clearly see the shape of the fringe frequencies matches their theoretical values.

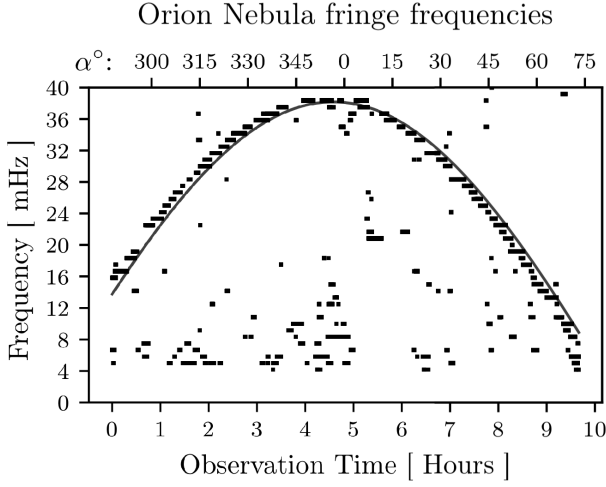


Figure 7: Found Orion Nebula fringe frequencies compared to theoretical fringe frequencies. The smooth line, the theoretical f_f were determined using Equation 26. The noisy data, the boxes, were found by applying a peak finder algorithm to the power spectra from Figure 4. Though the low signal to noise ratio is apparent, it is easy to see that the observed fringe frequencies follow the shape of the theoretical. A more intense source should allow for cleaner fringe frequencies.

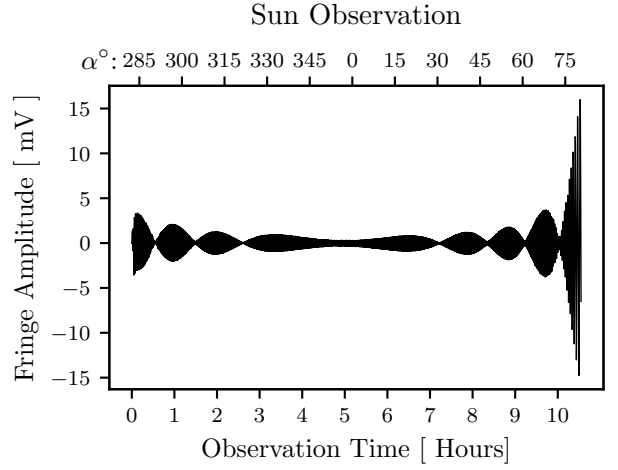


Figure 8: Fringe amplitudes collected during a 10 hour observation of the Sun. The fringe amplitudes are clearly modulated by some function that varies with hour angle, as the modulation mirrors about $\alpha = 0^\circ$. In an effort to eliminate a DC offset introduced by our equipment we subtract off the mean of the data. Note, the abrupt shape at the beginning of the observation is caused by the truncation of poor data. The discarded points all had near zero amplitude, and based on the position of the target at that time we believe the Oakland hills were occluding the Sun.

4 Resolved objects

4.1 Observations

For the resolvable objects, their right ascension and declination values change quickly. Our observing function takes this into account, recomputing these coordinates before finding the altitude and azimuth of the targets.

4.1.1 The Sun Observation

The brightest object in our sky, and one that emits strongly in the X-Band, the Sun makes an excellent target object. We observe the Sun for 10 hours, sampling the fringe amplitude every second. In Figure 8 we can see the fringe amplitudes being multiplied by some modulating function. The first 300 samples were discarded as the received data was of extremely poor quality. The altitude was very close to 5° and based on the azimuth we suspect the Sun was occluded by the Oakland hills.

4.1.2 The Moon observation

The second brightest object in the sky, the Moon emits some blackbody radiation and reflects light where illuminated by the Sun. We observe the Moon for just under 10 hours, sampling every second. In Figure 9 we see behavior similar to both the Orion Nebula observation and the Sun observation. We attribute these similarities to the low signal strength, like the Orion Nebula observation, and the resolved nature of the Moon, like the Sun observation. Towards the end of the observation we see that a sudden drop in amplitude, and after a short time, a sudden rise in amplitude. After analyzing the position of the Moon we conclude that a nearby building,

Evans Hall, occluded the Moon.

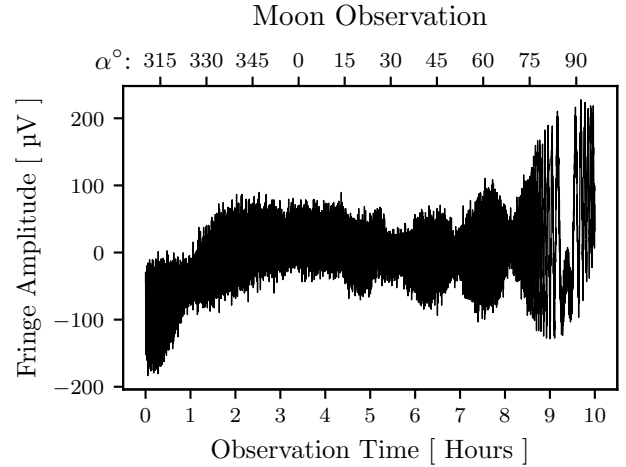


Figure 9: Fringe amplitudes collected during a observation of the Moon of just under 10 hours. Unlike the Sun observation, it is more difficult to see the Moon fringe amplitudes modulation. Here we again subtract off the mean of the data to reduce the DC offset. The data appears to exhibit features of both the Sun and Orion Nebula observations. At the start of the observation we see that general upwards trend from Figure 2, and from $\alpha^\circ = 30^\circ$ to $\alpha^\circ = 90^\circ$ the amplitudes are somewhat modulated. Note, the large dip towards the end of the observation may be caused by the Moon being occluded by a nearby building, Evans Hall.

4.2 Fringe Frequencies

4.2.1 Solar Fringe Frequencies

For our solar time series data we compute the power spectra much like in §3.2, with one small difference. The sun fringe amplitudes wave moderate banding effects we must account. The banding is the result of oscillations that are cut off at non-integer wavelengths. To reduce these we multiply each time window by a blackman signal filter of the same size. The blackman window suppresses data at the edges of frequency space, effectively highlighting frequencies in the center. The fringe frequencies are well defined in Figure 10.

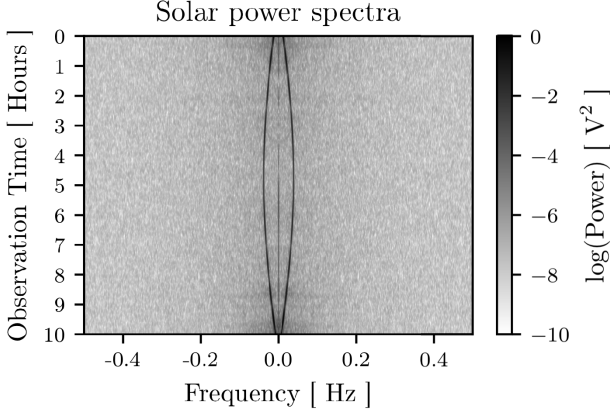


Figure 10: 36 000 spectra created from solar fringe amplitude windows, each 1200 seconds wide. As before we increment each row by one second. The time series windows are multiple by a blackman filter, which has the effect of broadening the peaks in the data. This is mitigated by the wide time window. The DC offset is still visible, though not as strongly as in the Orion Nebula spectra.

We also extract the actual fringe frequencies from the spectra plot and compare the to the theoretical values, using the process in 3.5 and find that they match very well. The peaks found for the sun exhibit no noise, though a curious step pattern is visible.

4.2.2 Lunar Fringe Frequencies

The lunar power spectra are computed is the same was as the solar fringe frequencies in §4.2.1. Though the Moon fringe amplitude signal strength is only a fraction of the Sun fringe amplitudes, the process works well. In Figure 12 the arcing lines are show the change in fringe frequency over time.

Figure 12 is created similarly to Figure 10, though the relatively high DC offset in the lunar data caused us to alter our peak finder algorithm. By dynamically adjusting the peak threshold we managed to extract low noise fringe frequencies that closely match the theoretical values.

4.3 Size

In theory our resolved sources are perfectly disk shaped with even intensity across their surfaces. Our interferometers are performing a Fourier transform of the sky, and the Fourier

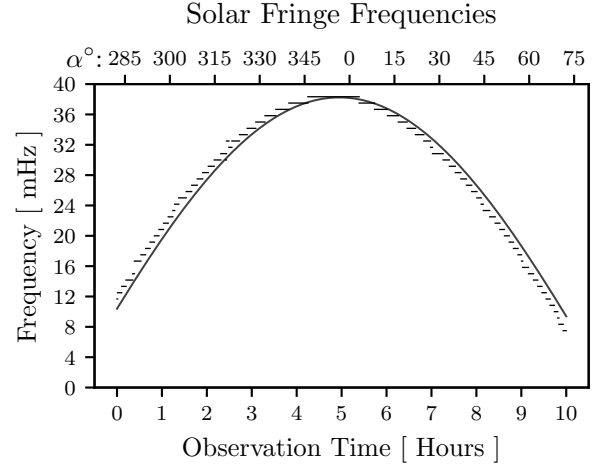


Figure 11: 36 000 fringe frequencies extracted from our power spectra data and the same number computed from theory. The data match quite well, though there is a curious quantization to the actual data. No reasonable answer was found as to the cause, though the non-continuous movement of the antennas was proposed. For subsequent work with solar fringe frequencies we will use the theoretical data since it is so close to the actual values, and the shape is smoother.

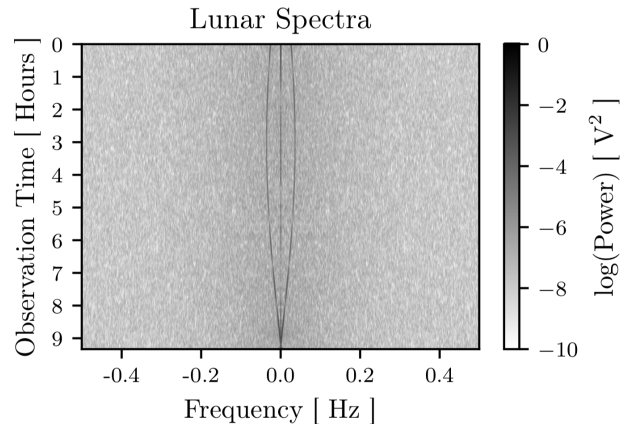


Figure 12: 34 800 power spectra created from lunar fringe amplitude windows, each 1200 seconds wide. As before we increment each window by one second. To suppress banding we multiply the time series windows by a blackman filter. We again see the line caused by the DC offset. Compared to Figure 10, the fringe frequencies are slightly more difficult to see, though they are well defined.

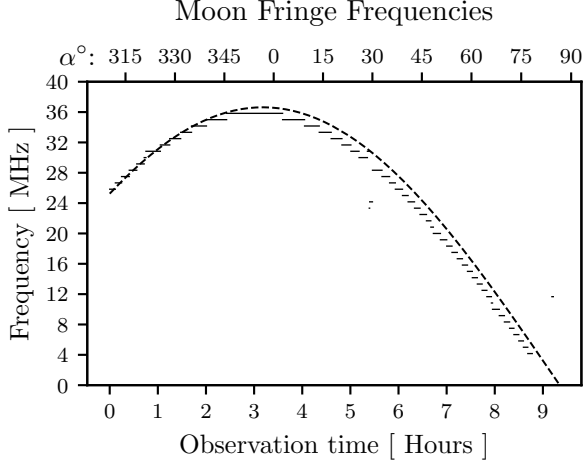


Figure 13: 34 800 lunar fringe frequencies extracted from the power spectra data using a descending threshold peak finder algorithm. The strong DC offset necessitated a very small threshold delta in the algorithm, and was rather slow. As seen in the other fringe frequency figures, the extracted values are lightly quantized, though they follow the shape of the theoretical values. The small amount of noise is due to the small threshold delta employed here. When the delta was near the value used for the Orion Nebular frequency extraction, the amount of noise increased noticeably

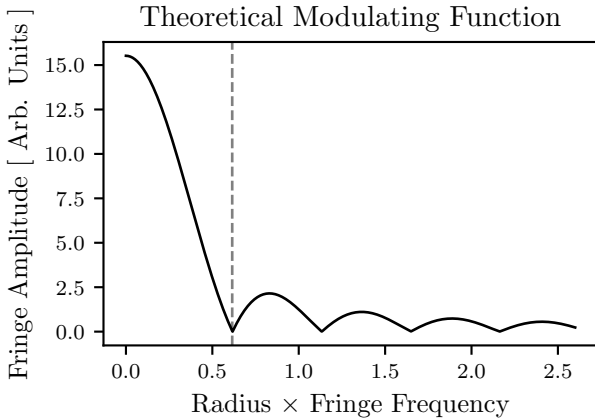


Figure 14: Theoretical modulating function with the point of the first minimum indicated. The modulating function (black) is computed with Equation 27. We find the first minimum to be at $\zeta = 0.615$. By comparing the location of this minimum with the corresponding location on the equivalent figures for our resolved sources we will be able to measure their angular radii

transform of a disk is a Bessel function of the first kind [3]. The fringe amplitude signal from perfect disk sources will be multiplied by this modulating function. A Bessel function representing these theoretical perfect disks can be written as

$$MF_{\text{theory}} \propto \sum_{n=-N}^{n=+N} \left[1 - \left(\frac{n}{N} \right)^2 \right]^{1/2} \cos \left(\frac{2\pi f_f R n}{N} \right). \quad (27)$$

In Equation 27, R is the radius of the source in radians, f_f is the fringe frequency in inverse radians, and we consider the intensity to be broken up into $2N + 1$ pieces, one for each hour angle. The Bessel function crosses zero repeatedly, and the value of its first crossing, ζ , can be used to find the radius of the disk.

$$R = \frac{\zeta}{f_f} \quad (28)$$

We expect our resolved sources to be only approximately disk shaped, due to intensity variation across the disk and irregular protuberances at the edge of the disk. For example, solar flares can project off the surface and sunspots alter the intensity. These variations away from a perfect disk mean the modulating function will not be exactly MF_{theory}

4.3.1 Solar Radius

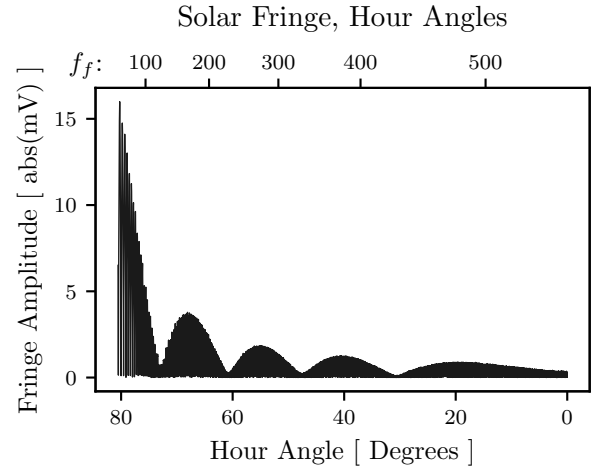


Figure 15: Absolute value of solar fringe amplitudes as a function of hour angle. The upper axis f_f are the corresponding solar fringe frequencies in cycles per radian. Both x axes are reversed to aid matching the minimums to our theoretical modulating function. We find the first minimum to occur at $f_f = 124.5$. Note, for this figure only data after hour angle = 0° was retained because our sampled fringe amplitudes from the beginning of the observation did not capture the necessary features.

To determine the first minimum required for Equation 28 we review to the solar fringe amplitudes in Figure 8. The fringe amplitudes have been modulated by our some function, which we take to be similar in shape to the theoretical modulating function MF_{theory} . The first portion of the observation does not have the initial drop to zero from a high amplitude, perhaps occluded by the Oakland hills as mentioned in §???. The end of the observation does have this feature, so we limit

our scope to fringe amplitudes corresponding to hour angles greater than 0° . In figure 15 we analyze the absolute value of these fringe amplitudes.

We find the first minimum occurs at $f_f = 124.5$ cycles/radian, so using Equation 28:

$$\begin{aligned} R_{\text{Sun}} &= \frac{0.615}{124.5/\text{radian}} \\ R_{\text{Sun}} &= 0.00494 \text{ radians} \\ R_{\text{Sun}} &= 0.28303^\circ \end{aligned} \quad (29)$$

If we consider the Sun to be a distance of 1 AU from the our interferometer, then simple geometry allows us to compute the radius of the Sun in kilometers.

$$\begin{aligned} R_{\text{Sun, km}} &= \sin(R_{\text{Sun}}) \cdot 1 \text{ AU} \cdot \frac{149\,597\,870.7 \text{ km}}{\text{AU}} \\ R_{\text{Sun, km}} &= 738\,900 \text{ km} \end{aligned} \quad (30)$$

When compared to the actual radius of the Sun, 695 508 km, we find our values have a 6% error. As mentioned in §4.3 we believe this may be caused by solar flare or sunspot phenomena.

4.3.2 Lunar Radius

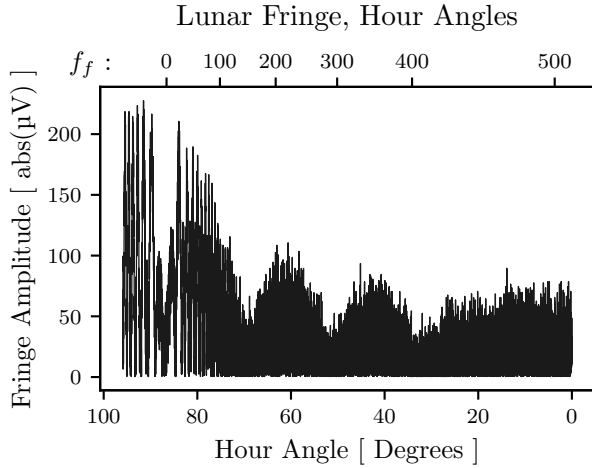


Figure 16: Absolute value of lunar fringe amplitudes as a function of hour angle. We reverse the x-axes to aid matching the minimums to our theoretical modulating function. We find the first minimum to occur at $f_f = 151$. We believe the dip from hour angle = 80° to 100° was caused by a nearby building, Evans Hall, occluding the moon. Note, for this figure only data after hour angle = 0° was retained because our sampled fringe amplitudes from the beginning of the observation did not capture the necessary features.

We find the first minimum occurs at $f_f = 151$ cycles/radian. Using Equation 28 we determine the angular radius of the Moon.

$$\begin{aligned} R_{\text{Moon}} &= \frac{0.615}{151/\text{radian}} = 0.00407 \text{ radian} \\ &= 0.23336^\circ \end{aligned} \quad (31)$$

The topocentric distance to the moon on the date of the observation was 365 030 km [1]. As in §4.3.1 we can compute the radius of the Moon in kilometers with geometry.

$$\begin{aligned} R_{\text{Moon, km}} &= \sin(R_{\text{Moon}}) \cdot 365\,030 \text{ km} \\ R_{\text{Moon, km}} &= 1486.7 \text{ km} \end{aligned} \quad (32)$$

This value differs from the actual value by approximately 14%. We believe this large variation can be largely attributed to the phase of the Moon on the date of the observation. The Moon was mid way through the waxing gibbous phase, and was 76.3% illuminated [1]. Additionally, the illumination in the X-Band may differ from the illumination in the visible spectrum. Furthermore, the relatively weak signal of the received fringe amplitudes may reduce resolution via a relative increase in noise.

5 Conclusions

The X-Band interferometer allowed us to make horizon to horizon observations of three celestial targets; the Sun, the Moon, and the Orion Nebula. With point source data we were able to classify the physical parameters of the interferometer, finding the difference in cable lengths to be $0.0103 \text{ cm} \pm 0.00003 \text{ m}$ and the direct baseline separation to be $14.815 \text{ m} \pm 0.003 \text{ m}$. By classifying the physical parameters of our interferometer we were able to compute the radii of the Sun and the Moon to within 6.24% and 14.43% of their true values. That such a straightforward interferometer design can accomplish this is remarkable. This system can calibrate its own baseline distances, compute the size of resolvable objects. With high precision baseline values it could map point sources in the sky by performing least square fits for those values. Having more antennas would allow you to assemble higher resolution data sets, and affording precision mapping.

6 Acknowledgements

Thank you to the authors of the lab writeup for holding our hands through the unfamiliar mathematics, and apologies to our readers for skipping most of the derivations. Thank you Deepthi for the vast amount of time she set aside to assist with the calculations of the object radii. For this project Amanda Fonseca kept us organized and on track, Steve Robinson provided valuable insights and sanity checks, Hayley Williams also provided sanity checks while I wrote the code for the observations and performed my own analysis. The code for this project will be available on my ugrad account and at <https://github.com/its2ez4u24get>, as soon as I get around to uploading it. The data is available by request at sheridan [at] berekely [dot] edu.

REFERENCES

- [1] Moon distance applet. <http://www.jgiesen.de/moondistance/index.htm>, 2018. Online; accessed 6 April 2018.
- [2] The orion nebula. <https://www.nasa.gov/feature/goddard/2017/messier-42-the-orion-nebula>, 2018. Online; accessed 6 April 2018.
- [3] Radio interferometry at x band. https://github.com/AaronParsons/ugradio/blob/master/lab_interf/interf.pdf, 2018. Online; accessed 6 April 2018.
- [4] Ifan G. Hughes and Thomas P. A. Hase. *Measurements and Their Uncertainties: A Practical Guide to Modern Error Analysis*. Oxford University Press, 2010.

Table 1: Interferometer parameters determined via brute force least squares fit to Orion Nebula fringe amplitudes.

	Interferometer Parameters			
	B_{ns}	B_{ew}	B_{direct}	Cable Differential
Distance [m]	1.436 ± 0.005	14.745 ± 0.001	14.815 ± 0.003	$.0103 \pm 0.00003$

Table 2: Start dates and times of our observations. The end time can be found using the observation duration. All samples were recorded using antennas at New Campbell Hall, University of California, Berkeley. Latitude 37.873199° , Longitude 1° , Altitude 120 m.

Target	UTC	Unix	Julian Date	Duration [seconds]
Orion Nebula	03/23/2018 8:49pm	1521838198.718769	2458201.367361	36277
Sun	03/10/2018 3:07pm	1520694461.9151909	2458188.129861	37966
Moon	03/27/2018 1:14am	1522113285.281195	2458204.551389	35998

Table 3: Object diameters. Comparison of the first minimum of the theoretical and actual amplitude modulation functions provides the radius in radians. We convert to diameter and present the result in multiple formats.

Object	Computed Object Diameter				Actual Diameter [km]	Percent Error
	Radians	Degrees	Arcseconds	Kilometers		
Sun	0.00988	0.56605	2037.8	1477900	1391000	6.24830
Moon	0.00814	0.46671	1680.2	3079.0	3474.8	14.429

Table 4: Signal chain components and their details.

#	Description	Frequency	Make	Model
1	Incoming signal	10.7 GHz	—	—
2	Double sideband mixer	—	—	—
2a	Local oscillator 1	8.75 GHz	HP	83630A Synthesized Sweeper
3	Double sideband mixer	—	—	—
3a	Local oscillator 2	1.37 GHz	Valon Technology	5008 Dual Frequency Synthesizer
4	Bandpass filter	312 MHz to 342 MHz	—	—
5	Double sideband mixer	—	—	—
5a	Local oscillator 3	327.5 MHz	Valon Technology	5008 Dual Frequency Synthesizer
6	Low pass filter	− 2 Hz to 2 Hz	—	—
7	Multiplier	—	—	—
8	Low pass filter	0.17 Hz	—	—
9	Output signal	—	HP	3478A Multimeter

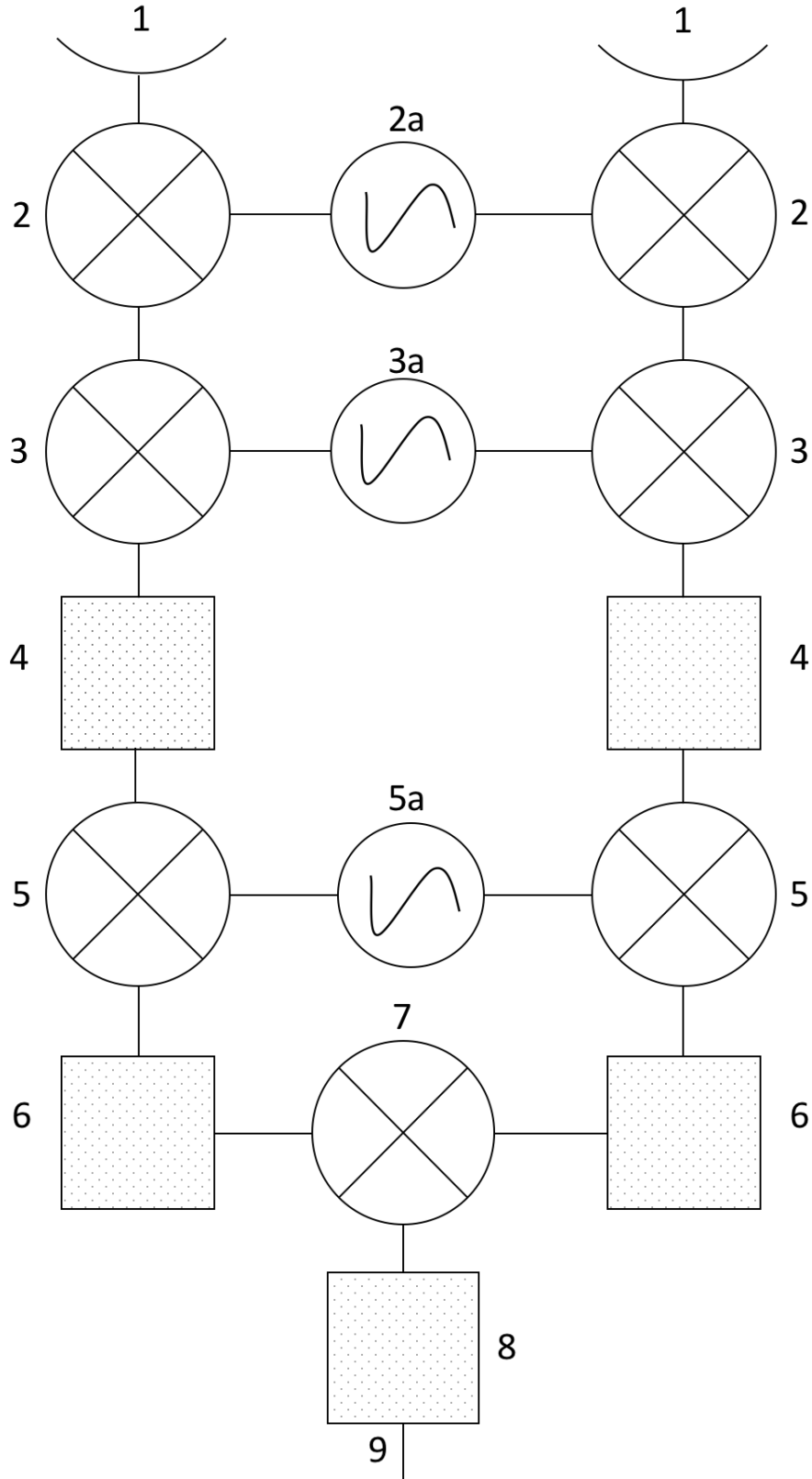


Figure 17: Signal chain diagram. For a description of the components see Table 4. X-band antennas are at the top and the signal chain output is at the bottom. The boxes with the dots are filters, while the circles with the x's inscribed are mixers. The circles with the stylized S are local oscillators.